

Communication

Very high surface area mesoporous thin films of SrTiO grown by pulsed laser deposition and application to efficient photoelectrochemical water splittingAbhijeet Laxman Sangle, Simrjit Singh, Jie Jian, Sneha Rohita
Bajpe, Haiyan Wang, Neeraj Khare, and Judith L. MacManus Driscoll*Nano Lett.*, **Just Accepted Manuscript** • DOI: 10.1021/acs.nanolett.6b02487 • Publication Date (Web): 24 Oct 2016Downloaded from <http://pubs.acs.org> on October 31, 2016**Just Accepted**

“Just Accepted” manuscripts have been peer-reviewed and accepted for publication. They are posted online prior to technical editing, formatting for publication and author proofing. The American Chemical Society provides “Just Accepted” as a free service to the research community to expedite the dissemination of scientific material as soon as possible after acceptance. “Just Accepted” manuscripts appear in full in PDF format accompanied by an HTML abstract. “Just Accepted” manuscripts have been fully peer reviewed, but should not be considered the official version of record. They are accessible to all readers and citable by the Digital Object Identifier (DOI®). “Just Accepted” is an optional service offered to authors. Therefore, the “Just Accepted” Web site may not include all articles that will be published in the journal. After a manuscript is technically edited and formatted, it will be removed from the “Just Accepted” Web site and published as an ASAP article. Note that technical editing may introduce minor changes to the manuscript text and/or graphics which could affect content, and all legal disclaimers and ethical guidelines that apply to the journal pertain. ACS cannot be held responsible for errors or consequences arising from the use of information contained in these “Just Accepted” manuscripts.

1
2
3 **Very high surface area mesoporous thin films of SrTiO₃ grown by pulsed laser**
4 **deposition and application to efficient photoelectrochemical water splitting**
5
6

7
8 Abhijeet Sangle^{†,*}, Simrjit Singh[§], Jie Jian[†], Sneha R. Bajpe[†], Haiyan Wang[†], Neeraj Khare[§]
9
10 and Judith L. MacManus-Driscoll^{†,*}

11
12 [†] Department of Materials Science and Metallurgy, University of Cambridge, Cambridge-
13 CB3 0FS, United Kingdom
14

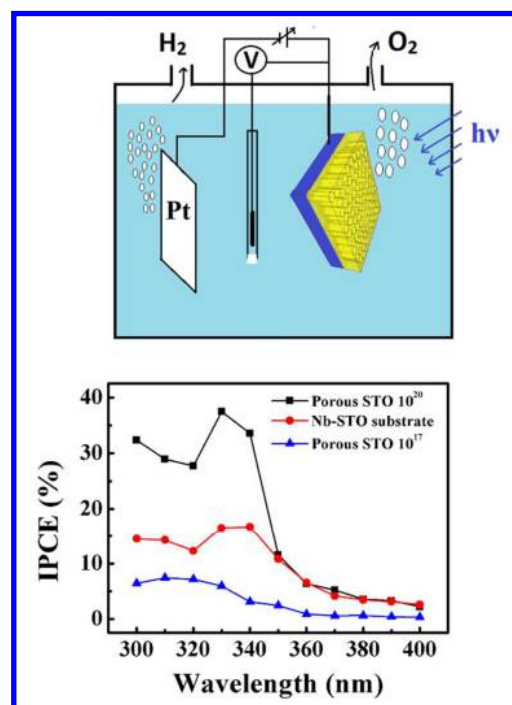
15
16 [§] Department of Physics, Indian Institute of Technology Delhi, New Delhi-110016, India
17

18
19 [†] Electrical and Computer Engineering 3128, Texas A & M University, College Station,
20 Texas 77843, United States
21

22
23 *Corresponding authors: as2174@cam.ac.uk, jld35@cam.ac.uk
24
25
26
27

28 Abstract: Very high surface area, self-assembled, highly
29 crystalline mesoporous SrTiO₃ (STO) thin films were
30 developed for photoelectrochemical water splitting.
31
32 Much improved performance of these mesoporous films
33 compared to planar STO thin films and any other form
34 of STO such as single crystal samples and
35 nanostructures was demonstrated. The high performance
36 resulted from very large surface area films and
37 optimisation of carrier concentration.
38
39

40
41
42
43
44
45
46
47
48 Keywords: Pulsed Laser Deposition, Self-assembled
49
50 nanocomposite films, Mesoporous crystalline thin films, High surface area films,
51
52 Photoelectrochemical water splitting, SrTiO₃
53
54
55
56
57
58
59
60



1
2
3 Since the discovery of photoelectrochemical water splitting using TiO_2 by Honda and
4
5 Fujishima¹, this type of renewable energy generation has captured the attention of the
6
7 researchers worldwide. There have been hundreds of different materials used by researchers
8
9 for this purpose. They can be broadly classified as transition metal chalcogenides, III-V
10
11 semiconductors, Group IV elemental and compound semiconductors, and transition metal
12
13 oxides. Except for a few, most of the photocatalyst materials suffer from one or more
14
15 drawbacks such as chemical instability²⁻⁷, environmental toxicity⁸, unfavourable band
16
17 positions³⁻⁵, overpotential loss⁹ or scarce availability leading to high costs¹⁰. Transition metal
18
19 oxides are the most widely researched group of photocatalysts and oxides, for example, STO
20
21 and BaSnO_3 have been shown to not be limited by the aforementioned drawbacks¹¹.
22
23 Wrighton *et al.*¹², in 1976, first demonstrated the usefulness of STO for light assisted water
24
25 splitting, thus making it the first material discovered to be suitable for photocatalytic water
26
27 splitting, without even applying any external bias¹³. Since then, STO has been shown to be an
28
29 effective photoelectrochemical (PEC) water splitting material. While STO absorbs only a
30
31 small portion of the visible light, impurity levels can be added in the bandgap to tune the
32
33 bandgap so it is more suitable for visible absorption. The visible light absorption of STO can
34
35 be improved by doping STO with metallic¹⁴⁻¹⁶ and non-metallic impurities^{17,18}. Moreover, the
36
37 performance can be further enhanced by growing tandem PEC cells, where STO is coated
38
39 with a suitable material with a bandgap in tandem to that of STO. The conduction band of
40
41 STO is 200 meV more negative than the conduction band of TiO_2 (anatase), making it
42
43 energetically more favourable for photo-assisted water splitting^{19,20}. In addition, STO has
44
45 excellent chemical and photochemical stability^{13,21-23} and high quality STO is reported to
46
47 have much higher electron mobility (5-8 $\text{cm}^2\text{V/s}$) compared to TiO_2 (0.1-4 $\text{cm}^2\text{V/s}$)²⁴. While
48
49 ZnO is a popular PEC water splitting material which has similar band positions to TiO_2 and is
50
51 easy to grow in nanostructured form, it too is inferior to STO since it undergoes
52
53
54
55
56
57
58
59
60

1
2
3 photocorrosion when put in an aqueous solution under UV light; it even gets corroded in the
4
5 dark when in an alkaline medium²⁵.
6
7

8 Many reports of using STO for photoelectrochemical water splitting are for materials
9
10 made in either bulk^{8,21} or nanopowder^{26–30} form. While nanopowders have the obvious
11
12 advantage over bulk form of higher surface area/volume ratio, thus increasing the number of
13
14 reaction sites for water splitting, they cannot be easily recovered from the electrolyte^{31–34}
15
16 Moreover, usually the nanopowders are coated with co-catalysts like Pt^{30,35,36}, IrO₂²⁷ or Au³⁷,
17
18 which act as cathodes for evolution of H₂. Not only are these co-catalysts expensive, but both
19
20 H₂ and O₂ gases evolve in close proximity^{23,34}, which is undesirable. Also, the co-catalysts
21
22 rob the photocatalysts of useful light-exposed surface²³. Finally, nanopowder STO
23
24 photocatalysts rely solely on photo-assisted water splitting without electric field assistance
25
26 for the hydrogen evolution process²⁶.
27
28
29
30

31 Many of the above disadvantages of using either bulk or nanopowder photocatalysts
32
33 can be eliminated if nanostructured photocatalysts are fixed to a conducting substrate, thus
34
35 making them easier to be recovered and reused. Also, gas separation is easier, as the anode
36
37 and cathode can be spatially separated. Some groups have coated nanopowders on conducting
38
39 substrates to immobilise them²⁶. However, the high surface area advantage offered by
40
41 nanopowders is lost if the nanopowders are simply coated on a conducting substrate, as the
42
43 specific surface area is substantially reduced. Moreover, because of the higher number of
44
45 grain boundaries and poor particle-to-particle contact in coated nanopowders, recombination
46
47 losses are higher.
48
49
50

51 A way to overcome the aforementioned problems of nanopowders is to use oriented,
52
53 substrate anchored nanotubes/nanorods. Such structures allow for directional charge carrier
54
55 transport offered without reduction of the surface area, as well as less recombination
56
57
58
59
60

1
2
3 losses^{20,31,38-43}. There are some investigations of oriented chemically grown mesoporous
4
5 films of SrTiO₃^{20,44-46}, but only one of those reports is for photoelectrochemical water
6
7 splitting and the performance is well below that of TiO₂²⁰. Improved performance is realised
8
9 in hydrothermally grown heterojunctions of TiO₂ nanotubes coated with STO^{20,47-49} (Table
10
11 1). Such heterojunctions give rise to cascading bandgaps, which leads to efficient charge
12
13 separation and reduced recombination losses leading to significantly better performance than
14
15 chemically grown plain STO films^{22,50-53} (Table 1).
16
17
18

19 As far as known, there are no reports of physical vapour deposited (PVD)
20
21 nanostructured or mesostructured STO films for PEC water splitting. On the other hand, such
22
23 films have strong potential for improved performance over chemically grown materials,
24
25 owing to their high crystalline perfection. Moreover, since there are no chemical reactions
26
27 taking place, there is lesser chance of by-product impurities from these reactions getting
28
29 incorporated in the films⁵⁴. Hence, lower defect concentrations are expected compared to
30
31 chemically grown nanostructures⁵⁵. Indeed, in chemically grown films, annealing at moderate
32
33 temperatures does not appreciably reduce the defect density^{56,57}. Another advantage of PVD
34
35 grown films is that they are very well-anchored to the substrate allowing for reuse many
36
37 times. Finally, as described in this work, use of new composite structures, allows for creation
38
39 of very high surface area films.
40
41
42
43

44 The aim of this work is to explore the photoelectrochemical water splitting performance
45
46 of PVD grown mesoporous thin films. Highly crystalline, well-oriented, epitaxial films of
47
48 STO with appropriate treatment to strongly increase surface area are used for this study. We
49
50 show much improved water splitting performance over previous reports on STO.
51
52

53 In brief, to create the mesoporous films, first columnar composite thin films of MgO
54
55 and STO were grown on Nb-STO (001) substrates (10 x 5 x 0.5 mm³ in size) using pulsed
56
57
58
59
60

laser deposition (PLD) (figure 1(a)). These films consist of epitaxial nanopillars (diameter ~ 20 nm) of MgO embedded in a matrix of STO (figure 1(b)). After fabrication of the composite films, the MgO phase was selectively etched out (figure 1(c)), leaving behind a high surface area honeycomb structure.

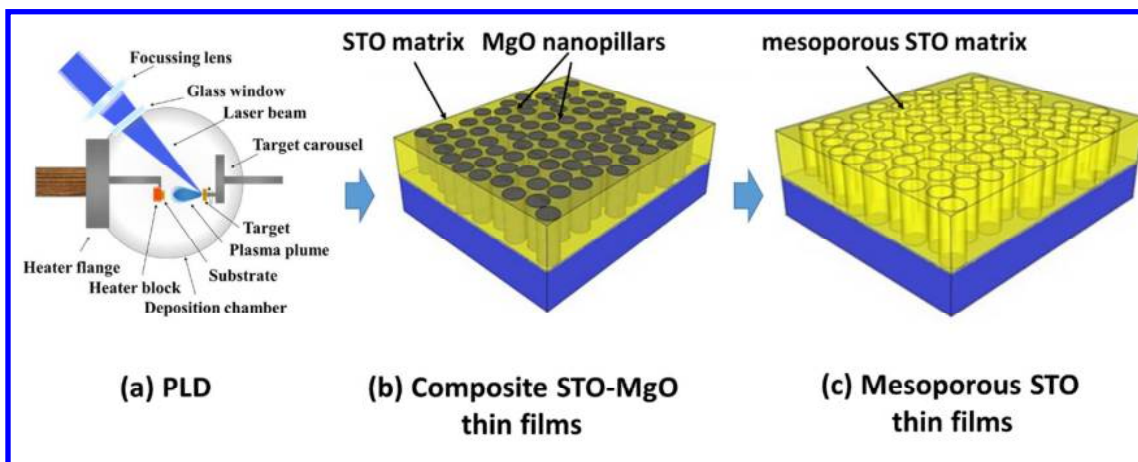


Figure 1: Schematic diagram showing (a) the PLD setup, (b) the PLD-grown columnar composite thin film containing STO matrix and MgO nanopillars and (c) the mesoporous STO thin film, after etching out the MgO nanopillars

Figure 2(a) is a plan-view SEM image of the composite thin film prior to etching, showing MgO nanopillars dispersed in the matrix of STO. The acidic etchant solution dissolves the alkaline MgO phase selectively, leaving the STO phase intact, as can be seen in Figure 2(b). Figure 2(c) shows an X-ray diffraction pattern of a composite film before and after etching the MgO nanopillars. From the 2θ - ω scans, it can be clearly seen that MgO grows with the same orientation as STO (001) single crystal. The STO film peaks overlap with the substrate peaks because of their very similar lattice parameter. We note, however, that the lattice parameters of the STO film and STO substrate are not necessarily identical owing to the vertical strain effects in the composite. The epitaxial quality of STO/MgO films grown on STO substrate is excellent, as we have shown in an earlier study⁵⁸. The MgO peak which was

present before etching is found to have disappeared after etching (Figure 2(c)). A cross-sectional TEM view of a typical mesoporous STO film is shown in Figure 2(d).

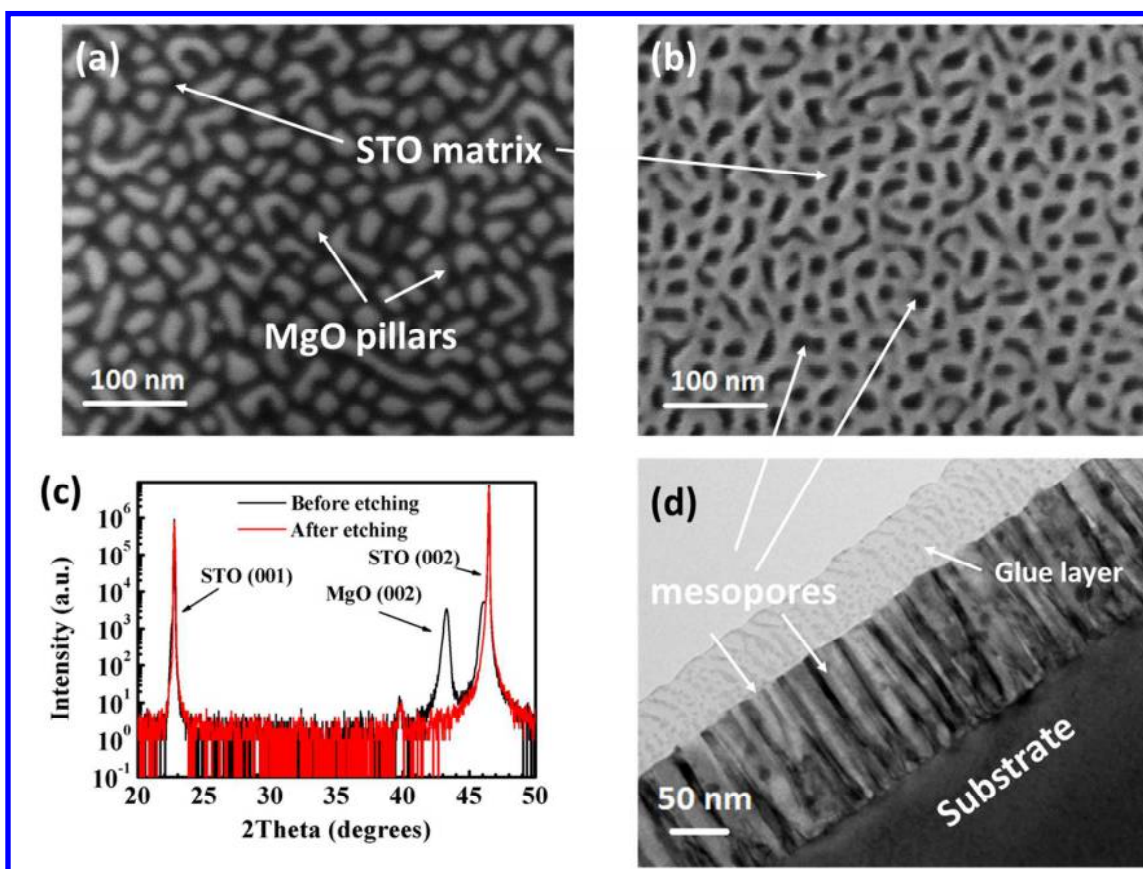
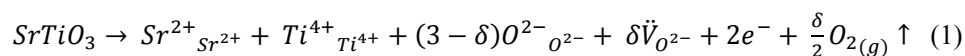


Figure 2: Plan-view SEM image of STO-MgO columnar composite thin film (a) before etching out the MgO nanopillars, and (b) after etching out the MgO nanopillars; (c) X-ray diffraction, out-of-plane 2θ - ω scans showing disappearing MgO peaks after etching, thus confirming the completion of the etching process, and (d) Cross-sectional TEM image of a typical porous STO thin film showing oriented mesopores (diameter ~ 20 nm). (As shown in the figure, the top layer is the glue layer used to glue the two pieces together before sample preparation).

From Figure 2(d), we can see that the mesopores are highly oriented in a direction perpendicular to the substrate surface. The SEM image (Figure 2(a)) shows that the mesopores are of diameter ~ 20 nm, and the wall-thickness of the surrounding STO is 5-7 nm.

1
2
3 This roughly translates to a 2500% increase in surface area over the surface of the substrate.
4
5 Comparing with mesoporous STO films of same thickness made by the hydrothermal
6
7 method⁵⁹, the mesoporous STO films of this study have ~ 5 times surface area.
8
9

10 The PLD grown films can be doped in a controlled manner⁶⁰ to achieve an optimum
11
12 carrier concentration, which is important for photoelectrochemical water splitting.
13
14 Stoichiometric STO has poor electrical conductivity and thus it is not suitable to act as a
15
16 photoelectrode, since the excited charge carriers need to be extracted easily for good water
17
18 splitting efficiency. The conductivity of STO can be increased by doping with donor
19
20 impurities such as Nb⁵⁺ or self-doping with oxygen^{22,61,62}. Oxygen vacancies are created by
21
22 annealing the material in a reducing environment^{33,61}, in accordance with equation (1) -
23
24



29
30 The oxygen vacancies act as shallow donors⁶³ and each vacancy donates two electrons.
31
32 This increases the charge carrier density in the semiconductor, and thus improves its
33
34 conductivity.
35
36

37 Results

38
39 Three mesoporous samples of different carrier concentration were studied – (a) a Nb-
40
41 STO substrate (as received), (b) a porous STO film post-annealed in high oxygen partial
42
43 pressure (400 mbar O₂), termed Porous STO 10¹⁷, and (c) a porous STO film post-annealed in
44
45 low oxygen partial pressure (0.2 mbar O₂), termed Porous STO 10²⁰. The above labelling of
46
47 the samples is based on their charge carrier concentrations (in number per cm³), which we
48
49 determine later.
50
51

52
53
54 The key photoelectrochemical water splitting results and the comparison of the
55
56 samples of this work with literature data are shown in Table 1. The first thing to note in Table
57
58
59
60

1 is that the different annealing conditions have brought about a three orders of magnitude of difference in charge carrier density from 10^{17} - 10^{20} cm^{-3} . A carrier concentration of the order of $\sim 10^{19}$ - 10^{20} cm^{-3} is normally desired for effective water splitting performance⁶⁴⁻⁶⁶. Hence, we have produced samples in this optimised carrier concentration range.

Table 1: Results of the measurements for the different samples of this work compared to other STO samples in the literature. V_{fb} is the flat band potential measured vs. the Ag/AgCl (3M KCl) reference electrode, N_{D} is the charge carrier density obtained $1/C^2$ vs. V plots (as discussed later). The incident photon to current efficiency (IPCE) was obtained at 0.5 V vs. Ag/AgCl (3M KCl).

	Sample	V_{fb} (V) vs. V(Ag/AgCl) (3M KCl) (V)	N_{D} (cm^{-3})	Highest values of IPCE
1.	Porous STO 10^{17} (this work)	-0.75	1.38×10^{17}	12% at 330 nm and 0.3 V vs. Ag/AgCl (3M KCl) (~ 1.30 V vs RHE)
2.	Porous STO 10^{20} (this work)	-0.60	2.80×10^{20}	38% at 330 nm and 0.3 V vs. Ag/AgCl (3M KCl) (~ 1.30 V vs. RHE)
3.	Nb-STO substrate (this work)	-1.00	1.90×10^{19}	16% at 330 nm and 0.3 V vs. Ag/AgCl (3M KCl) (~ 1.30 V vs. RHE)
4.	Colloidal suspension dip-coated Nb-doped STO thin film	-0.79	1.50×10^{20}	26% at 290 nm and at 1.23 V vs. RHE ²²
5.	Hydrothermally grown STO films decorated with carbon quantum dots	--	--	14% at 340 nm and at 1.23 V vs. RHE ⁵⁰
6.	Ir doped STO single crystals	-0.1 V vs. Ag/AgCl (0.4 V vs. RHE) (onset potential)		4% at 400 nm at 1 V vs. Ag/AgCl ⁶⁷ (~ 1.5 V vs. RHE)
7.	Hydrothermally grown STO-TiO ₂ heterostructures	-0.980 vs. (SCE) (~ 0.03 V vs. RHE)		6.55% at 360 nm and no external bias ²⁰
		--	--	27% at 330 nm and no external bias ⁴⁷
		-0.84 V (vs. SCE) or (~ -0.19 vs. RHE)	--	50% at 355 nm at 0.6 V vs. SCE ⁴⁸ (~ 1.25 V vs. RHE)

1
2
3 From Table 1, we can see that porous STO 10²⁰ shows much improved IPCE values
4
5 over the Nb-STO substrate and at 38% is one of the best efficiencies reported for plain STO
6
7 in the literature. Also, it is comparable to some of the highest results reported for STO-TiO₂
8
9 heterostructures^{47,48}.
10

11
12 In Table 1, the flat band potential (V_{fb}) values are also compared for the different
13
14 samples. V_{fb} is an important parameter for photoelectrochemical water splitting as it gives us
15
16 a direct measure of band bending in the sample, and hence it can tell us about the onset
17
18 potential. The V_{fb} for porous STO 10²⁰ is higher (more positive) than that for porous STO
19
20 10¹⁷. This can be explained by presence of surface states in porous STO 10²⁰ which are
21
22 absent or scarcely present in porous STO 10¹⁷. The high oxygen vacancy concentration leads
23
24 to high N_D . However, at the same time, generation of a high concentration of oxygen
25
26 vacancies means that the number of surface states is also high. A more detailed discussion
27
28 about V_{fb} and presence of surface states can be found in the supplementary information.
29
30
31
32
33
34
35
36
37
38
39
40
41
42
43
44
45
46
47
48
49
50
51
52
53
54
55
56
57
58
59
60

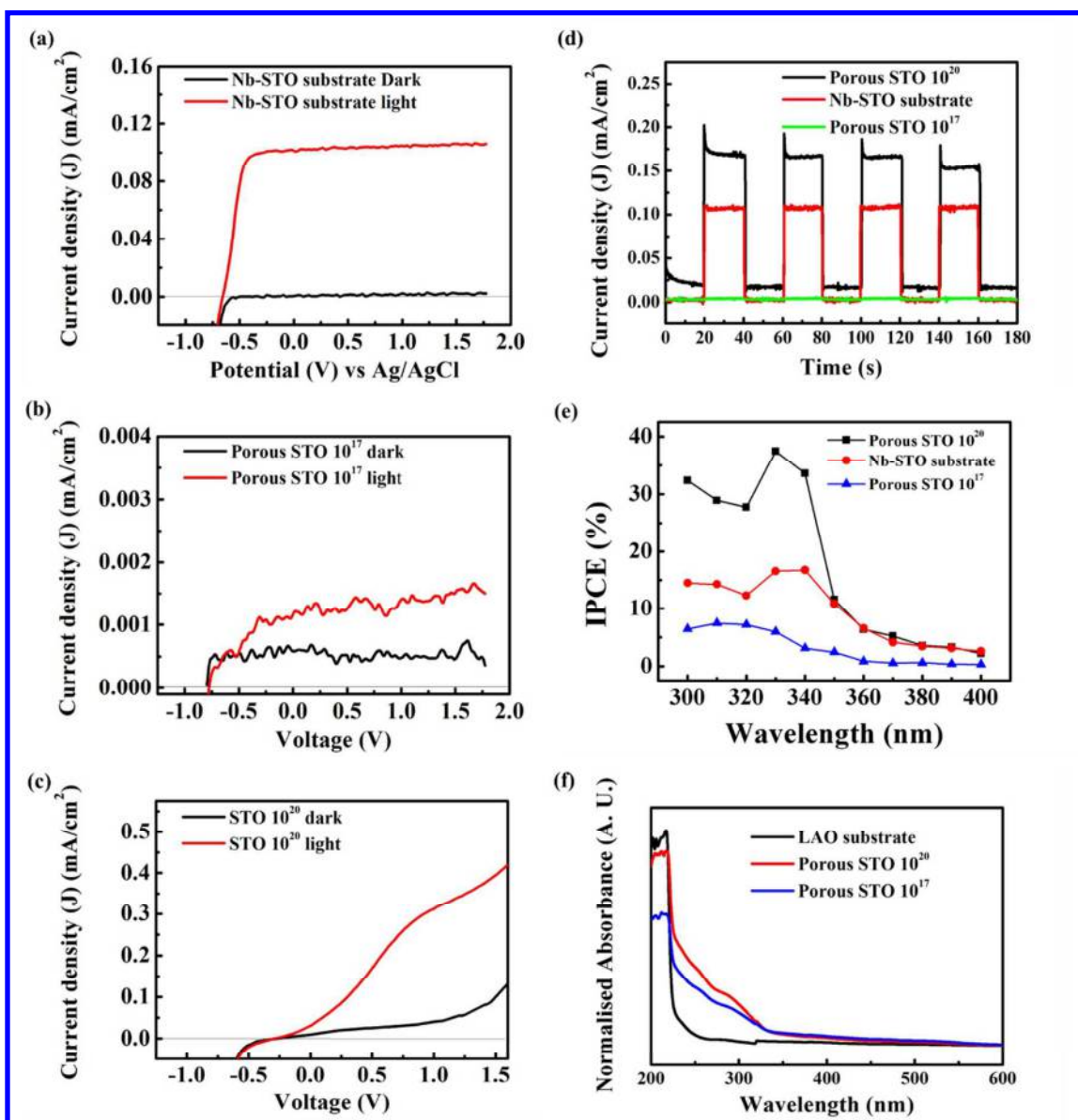


Figure 3: J-V characteristics of (a) Nb-STO substrate, (b) porous STO 10¹⁷ and (c) porous STO 10²⁰. (d) Chronoamperometry results of the samples. The potential used was 0.5 V vs. the Ag/AgCl (3M KCl) electrode for Chronoamperometry results. (e) Incident Photon to Current Efficiency (IPCE) results measured at 0.3 V vs. Ag/AgCl and (f) UV-Vis absorption spectra.

Now we look at the current density vs. applied potential (J-V) characteristics, comparing the photocurrent of all the three samples reported in this study. Figure 3 (a), (b)

1
2
3 and (c) show J-V characteristics of Nb-STO, porous STO 10^{17} and porous STO 10^{20} ,
4
5 respectively, in light and dark conditions. It can be clearly seen from Figure 3(a), (b) and (c)
6
7 that porous STO 10^{20} shows much improved photocurrent over the flat Nb-STO substrate.
8
9 This is consistent with the higher surface area and higher carrier concentration in porous STO
10
11 10^{20} . Also, as expected, the photocurrent is higher in porous STO 10^{20} than in porous STO
12
13 10^{17} on account of the better conductivity of porous STO 10^{20} . The current values are higher
14
15 than those achieved for STO thin films previously reported^{22,50}.
16
17

18
19 It can be seen that porous STO 10^{20} shows an onset of photocurrent at a slightly higher
20
21 voltage than that for the Nb-STO substrate. This can be explained by presence of surface
22
23 states in porous STO 10^{20} ^{68,69}. This phenomenon is discussed in detail in the supplementary
24
25 information. Porous STO 10^{17} shows negligible photocurrent compared to both porous STO
26
27 10^{20} and the Nb-STO substrate, consistent with the lower charge carrier concentration in
28
29 porous STO 10^{17} .
30
31

32
33 Figure 3 (d) shows the chronoamperometry results, measured at 0.5 V vs. Ag/AgCl
34
35 (3M KCl) and under a tungsten halogen lamp at 100 mW/cm^2 . As shown in the
36
37 supplementary information, the spectrum of the lamp has emission mainly in the visible and
38
39 infra-red region (500 nm – 1000 nm). Interestingly, the porous STO 10^{20} chronoamperometry
40
41 curves show spikes when the light is turned on before settling to a lower steady state current
42
43 value. This behaviour further supports the presence of surface states^{69–72}.
44
45
46

47 Figure 3(e) shows the Incident Photon to Current Efficiency (IPCE) values for the three
48
49 samples, measured at an applied bias of 0.3 V vs. Ag/AgCl. As expected for a large bandgap
50
51 semiconductor like STO (bandgap 3.2 eV), there is very little photocurrent from the visible
52
53 region of the light spectrum, and all three samples show low IPCE values at higher
54
55 wavelengths. However, for lower wavelengths corresponding to the UV region, we see that
56
57
58
59
60

1
2
3 porous STO 10²⁰ shows a much higher IPCE compared to both the Nb-STO substrate and
4
5 porous STO 10¹⁷. As reported in the literature^{73,74}, the IPCE curves peak at wavelengths
6
7 between 320 nm and 340 nm. The decrease of the efficiency values for wavelengths smaller
8
9 than 320 nm in non-passivated samples can be attributed to surface recombination losses^{13,73}.
10

11
12 Figure 3(f) shows the UV-vis absorption spectra of all the samples. Porous STO 10²⁰
13
14 shows slightly higher absorption closer to the band-edge of STO. This can be attributed to the
15
16 presence of oxygen vacancy states below the conduction band, thus permitting more light to
17
18 be absorbed in the visible range⁷⁵⁻⁷⁷. On the other hand, this higher absorption does not
19
20 translate into higher photocurrent in this range, as can be seen in the IPCE plots (Figure 3(e)).
21
22 The improvement in the efficiency is in the same wavelength range where it was showing
23
24 higher efficiency in the Nb-STO substrate. Hence, the oxygen vacancies only contribute
25
26 towards increasing the charge carrier density and not towards increasing the photocurrent
27
28 because of more absorption in the visible range. This is corroborated by several other
29
30 reports^{12,33,62}.
31
32
33
34

35
36 We now turn to analysis of the flat band potential (V_{fb}) and charge carrier density (N_D)
37
38 measurements. A high value (more negative) value of V_{fb} is beneficial to aid charge
39
40 separation and an optimum value of N_D is required for excellent electrical conductivity to
41
42 transport the separated charge carriers. The charge carrier density N_D and the flat band
43
44 potential V_{fb} are determined from $1/C^2$ vs. V plots. For the two samples porous STO 10¹⁷ and
45
46 Nb-STO substrate, the results were fairly linear (Figure 4(a) and 4(b)) and hence were fitted
47
48 as per the traditional Mott-Schottky equation⁷⁸:
49
50

$$\frac{1}{C^2} = \frac{2}{eA^2\epsilon_0\epsilon_r N_D} \left((V - V_{fb}) - \frac{\kappa T}{e} \right) \quad (2)$$

51
52
53
54
55 Where C is the capacitance of the semiconductor-electrolyte interface, e is the electronic
56
57 charge, A is the interfacial area, ϵ_0 is the permittivity of vacuum, ϵ_r is relative permittivity of
58
59
60

1
2
3 the semiconductor with respect to vacuum, N_D is the majority charge carrier density in the
4 semiconductor per cubic cm, V is the applied potential, V_{fb} is the flat band potential of the
5 semiconductor electrode in given electrolyte solution, κ is the Boltzmann's constant and T is
6 the temperature. For these plots, V_{fb} is determined from the x-intercept of the linear fits as per
7 the Mott-Schottky relation (eq. 2) and N_D is determined from the slope of these linear fits. In
8 this expression, we excluded the component $\kappa T/e$, because of its low value.
9

10 For the porous STO 10^{20} sample, the $1/C^2$ vs. V plots were non-linear and hence were fitted
11 to a quadratic expression (see Figure 4(c)). This expression is given in equation 3 below, and
12 it has been used previously for highly doped samples^{79,80}.
13
14

$$\frac{1}{C^2} = \frac{2}{e\epsilon_r\epsilon_0N_D A} (V - V_{fb}) + \frac{1}{b^2\epsilon_0^2} (V - V_{fb})^2 \quad (3)$$

15
16
17
18
19
20
21
22
23
24
25
26
27
28 Where all the symbols have the same meanings as for equation 2, except for b which is a
29 constant. From the parabolic fit of the data as per the equation above, values for V_{fb} and N_D
30 were approximately determined.
31
32
33
34
35
36
37
38
39
40
41
42
43
44
45
46
47
48
49
50
51
52
53
54
55
56
57
58
59
60

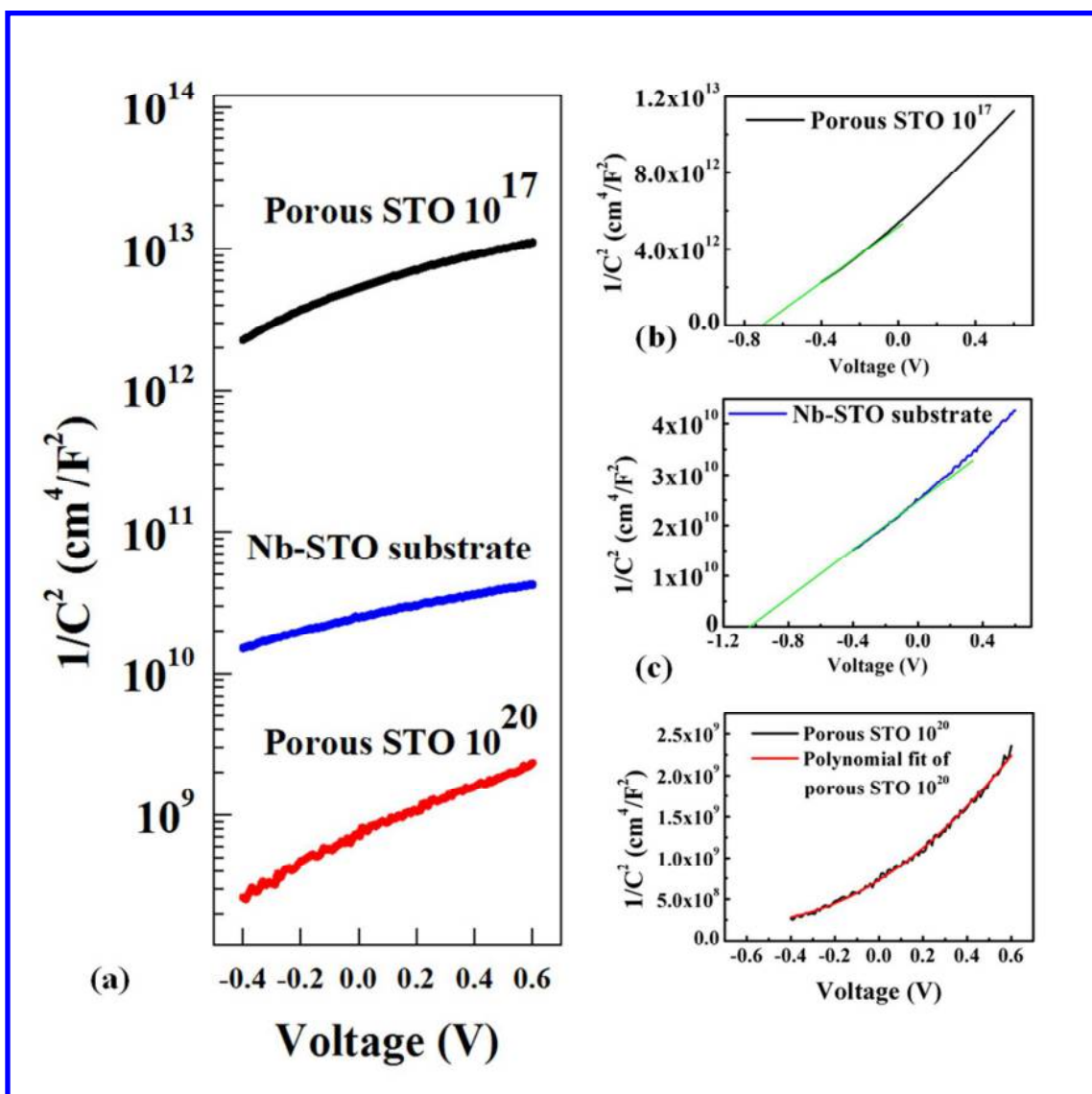


Figure 4: $1/C^2$ vs. V plots of various samples measured at 1 kHz with an amplitude of 10 mV. (a) The results for the three samples studied - porous STO 10²⁰, Nb-STO substrate and porous STO 10¹⁷ shown together in logarithmic scale, (b) and (c) Mott-Schottky linear fits of the results for porous STO 10¹⁷ and Nb-doped substrate, respectively and (d) polynomial fit of the results for porous STO 10²⁰.

All the samples showed a positive slope in the $1/C^2$ vs. V plots, thus confirming their n-type behaviour. From Figure 4(a), we can see that the $1/C^2$ values for porous STO 10¹⁷ are the highest at all biases, whereas those of porous STO 10²⁰ are the lowest. This indicates that

1
2
3 the effective capacitance of porous STO 10^{17} is much higher than that of porous STO 10^{20} ,
4
5 consistent with porous STO 10^{17} being much more resistive than porous STO 10^{20} . The
6
7 charge carrier density N_D is calculated from equation 2 using the slopes of the linear fits of
8
9 these plots. The x-intercepts of the linear fits give the values of V_{fb} , i.e., the applied bias at
10
11 which there is no band-bending⁷⁸. The values of V_{fb} and N_D are presented in Table 1.
12
13

14
15 N_D in porous STO 10^{17} was found to be lower than that of porous STO 10^{20} . Porous
16
17 STO 10^{20} showed an unexpectedly high flat band potential compared to the other samples.
18
19 This can be explained by presence of surface states from oxygen vacancy defects pinning the
20
21 Fermi level^{68,81–83}. As discussed in more detail in the supplementary section, electrochemical
22
23 impedance spectroscopy confirmed the presence of surface states in unpassivated porous
24
25 STO 10^{20} . It is well known that the photocurrent of oxygen-deficient samples can be
26
27 improved further by passivating the surface states with suitable chemicals like Al_2O_3 ^{68,70,84}.
28
29 Thus, perhaps the next step towards improving the PEC performance of these mesoporous
30
31 samples would be surface passivation by a very thin layer of Al_2O_3 .
32
33
34

35
36 To conclude, a very simple yet elegant method of growing highly oriented, epitaxial
37
38 crystalline, very high surface area mesoporous films with tunable electronic properties has
39
40 been demonstrated. The film shows very high photocatalytic performance. The approach
41
42 combines the benefits of using physical vapour growth to give very high quality, reusable
43
44 material with the benefits of having a very high surface area, which is normally only achieved
45
46 using chemical growth. Substrate-supported mesoporous structures are achieved by first
47
48 growing epitaxial columnar nanocomposite films, followed by selective etching out of one
49
50 phase. By carrier concentration tuning via doping, the oriented, mesoporous STO thin films
51
52 give very high efficiencies.
53
54
55
56
57
58
59
60

Experimental Section:

Fabrication: The columnar composite thin films of STO-MgO were deposited by laser ablation of a composite target containing STO and MgO. The targets were made by mixing and grinding STO and MgO nanopowders in equal weight proportion, followed by uniaxial pressing under 100kN for 10 minutes to form the pellets. The pellets were then sintered in oxygen flow rate of 40 sccm to 1100 °C for 6 hours. The laser energy used for the pulsed laser deposition of the thin films was $\sim 2 \text{ J/cm}^2$ and the laser pulse frequency was 1Hz. The Nb-STO substrates were heated to 770-800 °C, in an oxygen flow rate of 9.8 sccm with 0.2 mbar pressure inside the deposition chamber. The deposition rate was 10 nm/min. After the deposition, the films were annealed at 650 °C in situ at 400 mbar and 0.2 mbar of O₂ pressure for one hour, respectively, for porous STO 10¹⁷ and porous STO 10²⁰. To achieve a mesoporous STO film, the MgO phase was selectively etched out from the films by dipping them in 20% acetic acid solution at 60 °C for 30 minutes.

Characterisation: A four circle diffractometer was used for X-ray diffraction. A scanning electron microscope (SEM) was used to capture the surface images. The surface area of the mesoporous films was calculated using image analysis software to determine the average pore circumference from the plan-view SEM images. To compute the surface area of the pores, the values were multiplied by the number of pores, and the pore-length, which is equivalent to the film thickness. (Note: The area used for calculating photocurrent and IPCE data was the projected (plan-view) surface area under illumination for the sample, whereas for the $1/C^2$ vs. V plots, the area used was the estimated curved surface area of the nanowalls or cavities formed after etching out the nanocolumns. For simplicity, the area of the sample forming the 'cross-sections' of the nanowalls was ignored on account of being very small.). A photoelectrochemical work station coupled with a tungsten halogen lamp (Zahner WOW01) was used for photoelectrochemical characterisation. The lamp had very little UV component.

1
2
3 A comparison of the lamp's spectrum with the AM1.5 G is presented in the supplementary
4 information. The electrolyte used for the photoelectrochemical measurements was 0.5 M
5 NaOH solution. An in-house made photoelectrochemical cell with quartz windows and
6 polytetrafluoroethylene (PTFE) walls was used. A Pt wire as a counter electrode and an
7 Ag/AgCl (3M KCl) reference electrode were used for these measurements. The DC bias was
8 varied from -0.8 V to 1.8 V Ag/AgCl (3M KCl) for the J-V curves in both dark and light
9 conditions. The $1/C^2$ vs. V measurements were carried out from -0.4 V to 0.8 V vs. Ag/AgCl
10 (3M KCl) with an AC disturbance of 10 mV at 1 kHz. Electrochemical impedance
11 spectroscopy (EIS) measurements were performed for the frequency range 0.1 Hz to 1 kHz
12 and at 0V vs. Ag/AgCl (3M KCl) reference electrode. The EIS data was fitted using ZView
13 software suit. The IPCE data was recorded using a quantum efficiency measurement system
14 at 0.3 V vs. Ag/AgCl (3M KCl) electrode and in 0.5 M NaOH solution. A UV-VIS-NIR
15 spectrophotometer was for acquiring UV-Vis spectra from 200 nm to 800 nm. The films for
16 optical characterisation were grown on LaAlO₃ (001) single crystal substrates under the same
17 deposition conditions as used for the films grown on Nb-STO. The films used for UV-vis
18 spectroscopy were grown on LaAlO₃ because of its similar structure as that of Nb-STO,
19 which is essential for the heteroepitaxial growth of the two phases and because of the large
20 bandgap (5.2 eV) of LaAlO₃, thus allowing to detect any blue or red shifts in the band-edges
21 of these thin films.
22
23
24
25
26
27
28
29
30
31
32
33
34
35
36
37
38
39
40
41
42
43
44

45 Acknowledgements: We gratefully acknowledge the support from the Cambridge
46 Commonwealth Trust, ERC adg grant (247276) NOVOX and UKIERI grant
47 (IND/CONT/E/12-13/813). The TEM work at Texas A&M University is funded by the US
48 National Science Foundation (DMR-1401266). We also acknowledge the help from Y. J. Liu
49 and V. Kumar for the preliminary measurements for this project. We thank Dr. Oon Jew Lee
50 for her help during initial etching set up. We thank Mary Vickers for her help with the X-ray
51
52
53
54
55
56
57
58
59
60

1
2
3 diffraction. We thank Dr. Reza Saberi Moghaddam for his help with passivation related
4
5 matters. We thank Professor A. K. Cheetham for use of the UV-vis spectrophotometer in his
6
7 lab.
8
9

10 Associated Content: Supporting Information file. Plots of Electrochemical Impedance
11
12 Spectroscopy data, discussion of charge transfer mediated through surface states and band
13
14 bending, and emission spectrum of the lamp compared with the AM 1.5G spectrum.
15
16

17
18
19
20
21
22
23
24
25
26
27
28
29
30
31
32
33
34
35
36
37
38
39
40
41
42
43
44
45
46
47
48
49
50
51
52
53
54
55
56
57
58
59
60

References:

- (1) Fujishima, A.; Honda, K. *Nature* **1972**, *238* (5358), 37–38.
- (2) Woodhouse, M.; Parkinson, B. A. *Chem. Soc. Rev.* **2009**, *38* (1), 197–210.
- (3) Chandrasekaran, S.; McInnes, S. J. P.; Macdonald, T. J.; Nann, T.; Voelcker, N. H. *RSC Adv.* **2015**, *5* (104), 85978–85982.
- (4) Ashcheulov, P.; Kusko, M.; Fendrych, F.; Poruba, A.; Taylor, A.; Jager, A.; Fekete, L.; Kraus, I.; Kratochvilova, I. *Phys. Status Solidi A* **2014**, No. 10, 2347–2352.
- (5) Warren, E. L.; Boettcher, S. W.; McKone, J. R.; Lewis, N. S. **2010**, 7770, 77701F–77701F–7.
- (6) Price, M. J.; Maldonado, S. *J. Phys. Chem. C* **2009**, *113* (Figure 1), 11988–11994.
- (7) Hu, S.; Shaner, M. R.; Beardslee, J. A.; Lichterman, M.; Brunschwig, B. S.; Lewis, N. S. *Science* **2014**, *344* (6187), 1005–1009.
- (8) Rajeshwar, K. *J. Appl. Electrochem.* **2007**, *37* (7), 765–787.
- (9) Hu, J.; Zhu, F.; Matulionis, I.; Gaillard, N.; Deutsch, T.; Wang, H. In *White Papers on Materials for Photoelectrochemical Water Splitting*; 2013.
- (10) Prevot, M.; Sivula, K. *J. Phys. Chem. C* **2013**, *117* (17879–17893).

- 1
2
3 (11) Rajeshwar, K. In *Encyclopedia of Electrochemistry*; 2007.
4
5
6 (12) Wrighton, M. S.; Ellis, A. B.; Wolczanski, P. T.; Morse, D. L.; Abrahamson, H. B.;
7
8 Ginley, D. S. *J. Am. Chem. Soc.* **1976**, *98* (10), 2774–2779.
9
10
11 (13) Tomkiewicz, M.; Fay, H. *Appl. Phys.* **1979**, *18* (1), 1–28.
12
13
14 (14) Maruska, H. P.; Ghosh, A. K. *Sol. Energy Mater.* **1979**, *1* (3–4), 237–247.
15
16
17 (15) Tonda, S.; Kumar, S.; Anjaneyulu, O.; Shanker, V. *Phys. Chem. Chem. Phys.* **2014**, *16*
18 (43), 23819–23828.
19
20
21 (16) Wang, D.; Ye, J.; Kako, T.; Kimura, T. *J. Phys. Chem. B* **2006**, *110* (32), 15824–
22 15830.
23
24
25 (17) Wei, W.; Dai, Y.; Guo, M.; Yu, L.; Huang, B. *J. Phys. Chem. C* **2009**, *113*, 15046–
26 15050.
27
28
29 (18) Wang, J.; Li, H.; Li, H.; Yin, S.; Sato, T. *Solid State Sci.* **2009**, *11* (1), 182–188.
30
31
32 (19) Guo, K.; Liu, Z.; Wang, Y.; Zhao, Y.; Xiao, Y.; Han, J.; Li, Y.; Wang, B.; Cui, T. *Int.*
33 *J. Hydrogen Energy* **2014**, *39* (25), 13408–13414.
34
35
36 (20) Zhang, J.; Bang, J. H.; Tang, C.; Kamat, P. V. *ACS Nano* **2010**, *4* (1), 387–395.
37
38
39 (21) Mavroides, J. G.; Kafalas, J. A.; Kolesar, D. F. *Appl. Phys. Lett.* **1976**, *28* (5), 241–
40 243.
41
42
43 (22) Pinheiro, A. N.; Firmiano, E. G. S.; Rabelo, A. C.; Dalmaschio, C. J.; Leite, E. R. *RSC*
44 *Adv.* **2014**, *4* (4), 2029–2036.
45
46
47 (23) Wrighton, M. S. *Acc. Chem. Res.* **1979**, *12* (9), 303–310.
48
49
50 (24) Bera, A.; Wu, K.; Sheikh, A.; Alarousu, E.; Mohammed, O. F.; Wu, T. *J. Phys. Chem.*
51 *C* **2014**, *118* (49), 28494–28501.
52
53
54
55
56
57
58
59
60

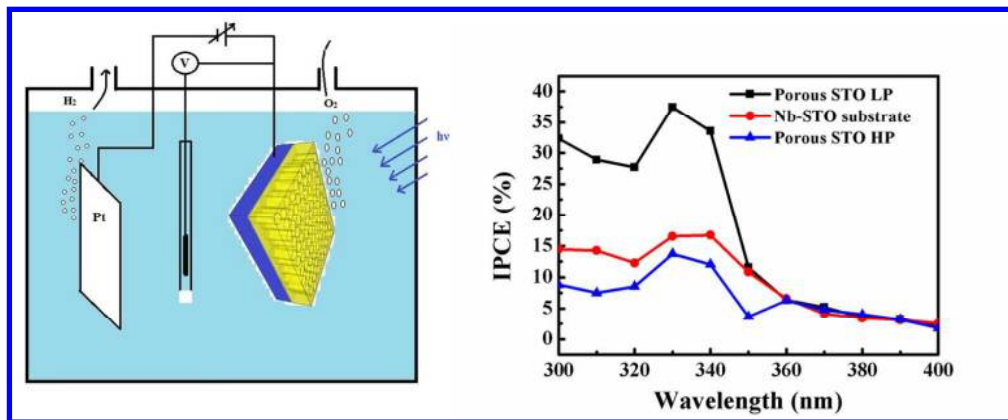
- 1
2
3 (25) Liu, M.; Nam, C.-Y.; Black, C. T.; Kamcev, J.; Zhang, L. *J. Phys. Chem. C* **2013**, *117*
4
5 (26), 13396–13402.
6
7
8 (26) Iwashina, K.; Kudo, A. *J. Am. Chem. Soc.* **2011**, *133* (34), 13272–13275.
9
10
11 (27) Asai, R.; Nemoto, H.; Jia, Q.; Saito, K.; Iwase, A.; Kudo, A. *Chem. Commun.* **2014**, *50*
12
13 (19), 2543–2546.
14
15
16 (28) Shen, P.; Lofaro, J. C. J.; Woerner, W. R.; White, M. G.; Su, D.; Orlov, A. *Chem. Eng.*
17
18 *J.* **2013**, *223*, 200–208.
19
20
21 (29) Niishiro, R.; Tanaka, S.; Kudo, A. *Appl. Catal. B Environ.* **2014**, *150–151*, 187–196.
22
23
24 (30) Liu, Y.; Xie, L.; Li, Y.; Yang, R.; Qu, J.; Li, Y.; Li, X. *J. Power Sources* **2008**, *183*
25
26 (2), 701–707.
27
28
29 (31) Paramasivam, I.; Jha, H.; Liu, N.; Schmuki, P. *Small* **2012**, *8* (20), 3073–3103.
30
31
32 (32) Zhang, X.; Huo, K.; Hu, L.; Wu, Z.; Chu, P. K. *J. Am. Ceram. Soc.* **2010**, *93* (9),
33
34 2771–2778.
35
36
37 (33) Wang, G.; Ling, Y.; Li, Y. *Nanoscale* **2012**, *4* (21), 6682.
38
39
40 (34) van de Krol, R.; Liang, Y.; Schoonman, J. *J. Mater. Chem.* **2008**, *18* (20), 2311.
41
42
43 (35) Puangpetch, T.; Sommakettarin, P.; Chavadej, S.; Sreethawong, T. *Int. J. Hydrogen*
44
45 *Energy* **2010**, *35* (22), 12428–12442.
46
47
48 (36) Puangpetch, T.; Sreethawong, T.; Yoshikawa, S.; Chavadej, S. *J. Mol. Catal. A Chem.*
49
50 **2009**, *312* (1–2), 97–106.
51
52
53 (37) Puangpetch, T.; Chavadej, S.; Sreethawong, T. *Energy Convers. Manag.* **2011**, *52* (5),
54
55 2256–2261.
56
57
58 (38) Baker, D. R.; Kamat, P. V. *Adv. Funct. Mater.* **2009**, *19* (5), 805–811.
59
60

- 1
2
3 (39) Innocenzi, P.; Malfatti, L. *Chem. Soc. Rev.* **2013**, *42* (9), 4198–4216.
4
5
6 (40) Bruce, P. G.; Scrosati, B.; Tarascon, J.-M. *Angew. Chem. Int. Ed. Engl.* **2008**, *47* (16),
7
8 2930–2946.
9
10 (41) Lee, U.; Min-Hye, K.; Young-Uk, K. *Bull. Korean Chem. Soc.* **2006**, *27* (6), 808–816.
11
12
13 (42) Schüth, F. *Chem. Mater.* **2001**, *13*, 3184–3195.
14
15
16 (43) Crepaldi, E. L.; Soler-Illia, G. J. D. A. A.; Grosso, D.; Cagnol, F.; Ribot, F.; Sanchez,
17
18 *C. J. Am. Chem. Soc.* **2003**, *125*, 9770–9786.
19
20
21 (44) Amani Hamedani, H.; Khaleel, J. A.; Dahmen, K.-H.; Garmestani, H. *Cryst. Growth*
22
23 *Des.* **2014**, *14* (10), 4911–4919.
24
25
26 (45) Xin, Y.; Jiang, J.; Huo, K.; Hu, T.; Chu, P. K. *ACS Nano* **2009**, *3* (10), 3228–3234.
27
28
29 (46) Liu, J.; Sun, Y.; Li, Z.; Li, S.; Zhao, J. *Int. J. Hydrogen Energy* **2011**, *36* (10), 5811–
30
31 5816.
32
33
34 (47) Yang, Y.; Lee, K.; Kado, Y.; Schmuki, P. *Electrochem. commun.* **2012**, *17*, 56–59.
35
36
37 (48) Jiao, Z.; Chen, T.; Yu, H.; Wang, T.; Lu, G.; Bi, Y. *J. Colloid Interface Sci.* **2014**, *419*,
38
39 95–101.
40
41
42 (49) Wu, Z.; Su, Y.; Yu, J.; Xiao, W.; Sun, L.; Lin, C. *Int. J. Hydrogen Energy* **2015**, *40*
43
44 (31), 9704–9712.
45
46
47 (50) Wang, F.; Liu, Y.; Ma, Z.; Li, H.; Kang, Z.; Shen, M. *New J. Chem.* **2013**, *37* (2), 290.
48
49
50 (51) Hertkorn, D.; Elsenheimer, H. C.; Bruch, R.; Paul, F.; Müller, C.; Hanemann, T.;
51
52 Reinecke, H. *J. Appl. Phys.* **2013**, *114* (2), 27020.
53
54
55 (52) Zhao, L.; Fang, L.; Dong, W.; Zheng, F.; Shen, M.; Wu, T. *Appl. Phys. Lett.* **2013**, *102*
56
57 (12), 121905.
58
59
60

- 1
2
3 (53) Katayama, M.; Ishihara, T.; Matsumoto, Y.; Kubota, J.; Domen, K. In *218th*
4
5 *Electrochemical Society Meeting*; 2010.
6
7
8 (54) Willmott, P. R.; Huber, J. R. *Rev. Mod. Phys.* **2000**, *72* (1), 315–328.
9
10 (55) Djurišić, A. B.; Tam, K. H.; Cheung, C. K.; Leung, Y. H.; Ling, C. C.; Beling, C. D.;
11
12 Fung, S.; Chan, W. K. In *Nanoscale Phenomena: Basic Science to Device*
13
14 *Applications*; Springer Science & Business Media, 2007; pp 117–130.
15
16
17 (56) Jiao, Z.; Chen, T.; Xiong, J.; Wang, T.; Lu, G.; Ye, J.; Bi, Y. *Sci. Rep.* **2013**, *3*, 2720.
18
19
20 (57) Das, R.; Kumar, A.; Kumar, Y.; Sen, S.; Shirage, P. M. *RSC Adv.* **2015**, *5* (74), 60365–
21
22 60372.
23
24
25 (58) Zhang, W.; Chen, A.; Bi, Z.; Jia, Q.; Macmanus-Driscoll, J. L.; Wang, H. *Curr. Opin.*
26
27 *Solid State Mater. Sci.* **2014**, *18* (1), 6–18.
28
29
30 (59) Sun, Y.; Liu, J.; Li, Z. *J. Solid State Chem.* **2011**, *184* (8), 1924–1930.
31
32
33 (60) Krebs, H.; Weisheit, M.; Erik, S.; Scharf, T.; Fuhse, C.; St, M.; Sturm, K.; Seibt, M.;
34
35 Kijewski, H.; Nelke, D.; Panchenko, E.; Buback, M. *Adv. Solid State Phys.* **2003**, *43*,
36
37 505–518.
38
39
40 (61) Jin, K. X.; Li, Y. F.; Wang, Z. L.; Peng, H. Y.; Lin, W. N.; Kyaw, a. K. K.; Jin, Y. L.;
41
42 Jin, K. J.; Sun, X. W.; Soci, C.; Wu, T. *AIP Adv.* **2012**, *2* (4), 0–9.
43
44
45 (62) Tan, H.; Zhao, Z.; Zhu, W.; Coker, E. N.; Li, B.; Zheng, M.; Yu, W.; Fan, H.; Sun, Z.
46
47 *ACS Appl. Mater. Interfaces* **2014**, *6* (21), 19184–19190.
48
49
50 (63) Liu, M.; Lyons, J. L.; Yan, D.; Hybertsen, M. S. *Adv. Funct. Mater.* **2015**, n/a-n/a.
51
52
53 (64) Fu, Z.; Jiang, T.; Liu, Z.; Wang, D.; Wang, L.; Xie, T. *Electrochim. Acta* **2014**, *129*,
54
55 358–363.
56
57
58
59
60

- 1
2
3 (65) Wang, C.; Chen, Z.; Jin, H.-B.; Cao, C.; Li, J.; Mi, Z. *J. Mater. Chem. A* **2014**,
4
5
6 (66) Tamura, H.; Yoneyama, H.; Iwakura, C.; Sakamoto, H.; Murakami, S. *J. Electroanal.*
7
8 *Chem. Interfacial Electrochem.* **1977**, *80*, 357–363.
9
10 (67) Kawasaki, S.; Takahashi, R.; Akagi, K.; Yoshinobu, J.; Komori, F.; Horiba, K.;
11
12 Kumigashira, H.; Iwashina, K.; Kudo, A.; Lippmaa, M. *J. Phys. Chem. C* **2014**, *118*,
13
14 20222–20228.
15
16 (68) Liu, R.; Zheng, Z.; Spurgeon, J.; Yang, X. *Energy Environ. Sci.* **2014**, 2504–2517.
17
18 (69) Le Formal, F.; Tétreault, N.; Cornuz, M.; Moehl, T.; Grätzel, M.; Sivula, K. *Chem. Sci.*
19
20 **2011**, *2* (4), 737.
21
22 (70) Le Formal, F.; Sivula, K.; Grätzel, M. *J. Phys. Chem. C* **2012**, *116* (51), 26707–26720.
23
24 (71) Peter, L. M.; Li, J.; Peat, R. *J. Electroanal. Chem.* **1984**, *165* (1–2), 29–40.
25
26 (72) Wolcott, A.; Smith, W. a; Kuykendall, T. R.; Zhao, Y.; Zhang, J. Z. *Small* **2009**, *5* (1),
27
28 104–111.
29
30 (73) Mavroides, J. G.; Kafalas, J. a.; Kolesar, D. F. *Appl. Phys. Lett.* **1976**, *28* (5), 241–243.
31
32 (74) Rajeshwar, K.; Singh, P.; DuBow, J. *Electrochim. Acta* **1978**, *23* (11), 1117–1144.
33
34 (75) Yin, J.; Ye, J.; Zou, Z. *Appl. Phys. Lett.* **2004**, *85* (4), 689–691.
35
36 (76) Kumar, A.; Dho, J. *Curr. Appl. Phys.* **2013**, *13* (4), 768–774.
37
38 (77) Mochizuki, S.; Fujishiro, F.; Ishiwata, K.; Shibata, K. *Phys. B Condens. Matter* **2006**,
39
40 376–377 (1), 816–819.
41
42 (78) Gelderman, K.; Lee, L.; Donne, S. W. *J. Chem. Educ.* **2007**, *84* (4), 685.
43
44 (79) Suzuki, S.; Yamamoto, T.; Suzuki, H.; Kawaguchi, K.; Takahashi, K.; Yoshisato, Y. *J.*
45
46 *Appl. Phys.* **1997**, *81* (10), 6830.
47
48
49
50
51
52
53
54
55
56
57
58
59
60

- 1
2
3 (80) Matsumoto, Y.; Takata, S.; Tanaka, R.; Hachiya, A. *J. Appl. Phys.* **2011**, *109* (1),
4
5 14112.
6
7
8 (81) Nagasubramanian, G.; Wheeler, B. L.; Fan, F.-R. F.; Bard, A. J. *J. Electrochem. Soc.*
9
10 **1982**, *129* (10), 2224.
11
12
13 (82) Abruña, H. D. *J. Electrochem. Soc.* **1982**, *129* (10), 2224.
14
15
16 (83) Pyper, K. J.; Yourey, J. E.; Bartlett, B. M. *J. Phys. Chem. C* **2013**, *117*, 24726–24732.
17
18
19 (84) Hwang, Y. J.; Hahn, C.; Liu, B.; Yang, P. *ACS Nano* **2012**, *6* (6), 5060–5069.
20
21
22
23
24
25
26
27
28
29
30
31
32
33
34
35
36
37
38
39
40
41
42
43
44
45
46
47
48
49
50
51
52
53
54
55
56
57
58
59
60



Very high surface area mesoporous thin films grown by pulsed laser deposition (PLD) for photoelectrochemical water splitting

Very high surface area mesopor
411x166mm (96 x 96 DPI)